Materials Today Bio 29 (2024) 101359

Contents lists available at ScienceDirect

Materials Today Bio

journal homepage: www.journals.elsevier.com/materials-today-bio

Multifunctional layered microneedle patches enable transdermal angiogenesis and immunomodulation for scarless healing of thermal burn injuries

Hang Chen [a,1], Lu Tan [a,1], Liqi Li [b,1], Yan Zheng [a], Menghuan Li [c], Shuohan He [a], Zhong Luo [a,c,*], Kaiyong Cai [a,**], Yan Hu [a,***]

[a] Key Laboratory of Biorheological Science and Technology, Ministry of Education, College of Bioengineering, Chongqing University, Chongqing, 400044, China
[b] Department of General Surgery, Xinqiao Hospital, Army Medical University, Chongqing, 400037, China
[c] School of Life Science, Chongqing University, Chongqing, 400044, China

ARTICLE INFO

Keywords:
Layered microneedle
Hypoxia-induced exosomes
Angiogenesis
Anti-inflammatory
Burn healing

ABSTRACT

Thermal burn injuries induce substantial alterations in the immune compositions and anatomical structures in the skin, which are characterized by strong inflammatory responses and thick eschar formation on the wound surface. These traits challenge current treatment paradigms due to insufficient drug penetration into affected tissues and the unsatisfactory wound regeneration. Herein, we report a layered microneedle (MN) patch for addressing these challenges in burn injury healing. The MN patch features a core/shell structure with methacrylated gelatin (GelMA) encapsulated with human umbilical vein endothelial cell (HUVECs)-derived hypoxia-induced exosomes (EXO-H) as the bottom layer and sodium alginate (SA) containing naringin (Nar)-loaded $CaCO_3$ nanoparticles ($CaCO_3$@Nar) as the top layer. Upon administration onto thermal burn injury site, the MN patches enable transdermal drug delivery by perforating the eschar. The spontaneous degradation of $CaCO_3$@Nar in the interstitial fluid triggers sustained Nar release to alleviate local inflammation and scavenge excessive reactive oxygen species (ROS). Meanwhile, EXO-H significantly promote the migration and proliferation of HUVECs and enhance their angiogenesis capacity to support scarless wound tissue regeneration. The MN patch in this work successfully promoted scarless healing of skin burn injuries on rat models, providing an approach for thermal burn treatment in the clinics.

1. Introduction

Thermal burns are common skin injuries that can be caused by the excessive heat [1]. However, the effective treatment of thermal burns still remains a major challenge in the clinics. Specifically, thermal burns could substantially impair the structural and functional integrity of the skin tissues, establishing areas with high inflammation status and limited blood circulation [2]. These traits make the thermal burn wound difficult to heal with long rehabilitation period and high risk of scar formation [3–5]. Therefore, it is often necessary to apply additional pro-angiogenesis and anti-inflammation modalities to accelerate burn injury healing. Nevertheless, the eschar formed on the wound surface proves a formidable barrier that limit the penetration of these therapeutic agents, which substantially impairs the repair efficacy of deep wounds [6]. Consequently, new technologies are urgently needed to mediate transdermal drug delivery at the burn injury site for boosting wound regeneration.

Microneedle array patches are an innovative technology to improve the penetration efficiency of various drugs through the skin barrier, which has attracted significant clinical attention for both local and systemic drug delivery [7]. From a general perspective, microneedle patches are essentially flexible sheets embedded with a densely packed

* Corresponding author. Key Laboratory of Biorheological Science and Technology, Ministry of Education, College of Bioengineering, Chongqing University, Chongqing, 400044, China.
** Corresponding author.
*** Corresponding author.
E-mail addresses: luozhong918@cqu.edu.cn (Z. Luo), kaiyong_cai@cqu.edu.cn (K. Cai), huyan303@cqu.edu.cn (Y. Hu).
[1] These authors contributed equally to this work.

https://doi.org/10.1016/j.mtbio.2024.101359
Received 8 June 2024; Received in revised form 22 October 2024; Accepted 21 November 2024
Available online 22 November 2024

array of microscale sharp needles, which could easily penetrate the stratum corneum and other pathological formations, leading to enhanced release of bioactive contents into the underlying tissues via passive or assisted diffusion [8,9]. In addition, the recent advances in material science and technology enable the facile integration of a broad spectrum of therapeutic agents of synthetic and biological origins including small-molecule drugs, nucleotides and exosomes, further expanding their potential application as tailorable drug depots for treating various skin or systemic diseases [10,11]. However, microneedle patches with cooperative pro-angiogenesis and anti-inflammation capabilities for thermal burn injury treatment are still rare.

Based on the merits above, here we propose a biofunctional layered microneedle (MN) patch that enable transdermal delivery of bioactive agents for treating thermal burn injuries, which is realized through the cooperative in-situ immunomodulation and angiogenesis (Fig. 1). For this purpose, we first extracted exosomes from hypoxia-conditioned HUVECs and loaded them into crosslinked methacrylated gelatin (GelMA) matrices, which were subsequently processed into planar shapes with ordered microneedle arrays as the bottom substrate. Previous studies confirmed that exosomes secreted by hypoxic endothelial cells could upregulate Lysyl oxidase-like 2 (LOXL2) and miR-30a-5p to promote extracellular matrix (ECM) remodeling in peripheral tissues as well as stimulating H19 expression, leading to accelerated wound regeneration and vascularization for scarless wound healing [12,13]. On the other hand, naringin (Nar) molecules, a natural flavonoid compound

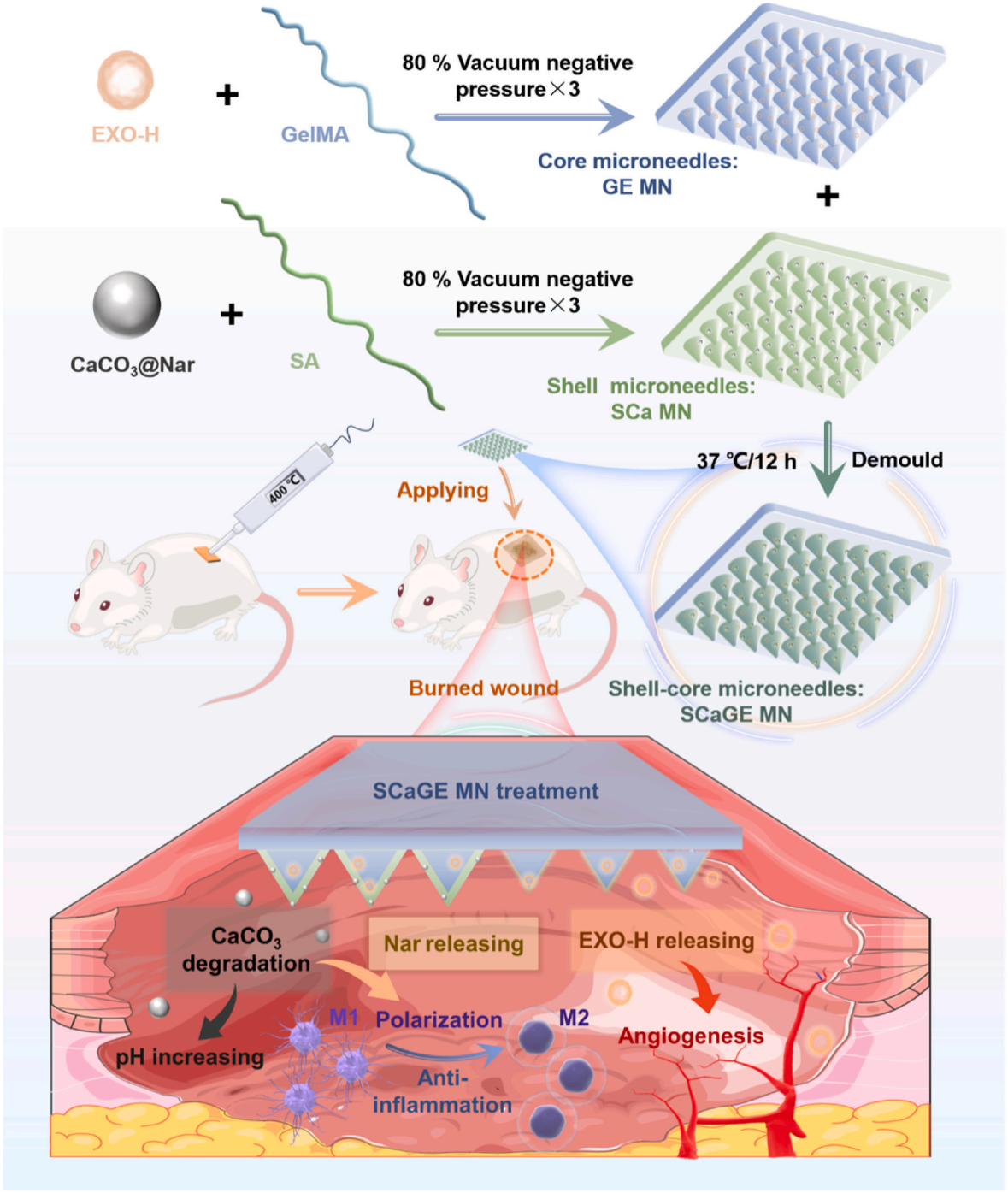

Fig. 1. Schematic illustrations of the preparation and application of layered MN patches for promoting scarless healing of thermal burn wounds.

with potent antioxidative and anti-inflammatory capabilities, were integrated into $CaCO_3$ nanosubstrates through biomineralization to form $CaCO_3$@Nar nanoparticles, which were further embedded into sodium alginate (SA) matrices and anchored onto the GelMA-based microneedle arrays as the top layer without altering the microneedle morphology [14]. After administration onto the thermal burn wounds, the microneedles could easily puncture the eschar and establish firm contact with the underlying tissues, thus potentiating gradual release of hypoxia-induced exosomes (EXO-H) and $CaCO_3$@Nar NPs across all layers of affected skin tissues. The spontaneous hydrolysis of $CaCO_3$@Nar NPs in the interstitial fluids would trigger the release of Nar molecules to relieve the excessive inflammation reactions in the wound bed, while EXO-H could promote local angiogenesis while remodel ECM to accelerate wound regeneration and prevent scar formation. In vivo analysis on thermal burn-bearing Sprague-Dawley (SD) rat models showed that the MN patches could substantially shorten the rehabilitation period of severe thermal burns of skin and avoid scar formation at the wound site, providing an approach for thermal wound management in the clinics.

2. Materials and method

2.1. Materials

Type A gelatin (sourced from porcine skin) was purchased from Sigma-Aldrich (USA). Methyl methacrylate (MA) was purchased from Beijing Beiling Technology Co., Ltd. (China). Acetone was obtained from Chongqing Chuandong Chemical Co., Ltd. (China). Sodium alginate (SA) was purchased from Shanghai Aladdin Bio-Chem Technology Co., Ltd. (China). Cell Counting Kit-8 (CCK-8) was purchased from Solarbio Biotechnology Co., Ltd. (China). ELISA kit was purchased from ABclon (China). BCA Protein Concentration Assay Kit was purchased from Beyotime Biotechnology (China). Rabbit polyclonal antibodies against CD86 and CD206 were purchased from Shanghai Sangon Biotechnology Co., Ltd. (China). High glucose DMEM powder culture medium was purchased from Gibco (USA). The reagents were analytically pure and used as received.

2.2. Cell culture and animal handling

HUVECs and RAW246.7 cells were cultured in high-glucose medium containing 10 % fetal bovine serum and 1 % penicillin-streptomycin. The incubator was set at 37 °C with 5 % CO_2. Male Sprague-Dawley (SD) rats with an average body weight of 280–320 g were produced by Hunan SJA Laboratory Animal Co., Ltd. (Hunan, China). The housing and operation procedures were reviewed and approved by the Animal Care and Use Committee of Chongqing University.

2.3. Synthesis and characterization of $CaCO_3$@Nar

We prepared $CaCO_3$@Nar nanoparticles using the previously reported one-pot gaseous diffusion method [15]. 150 mg of anhydrous calcium chloride and 150 mg of sodium alginate were dissolved in 100 mL of anhydrous ethanol, 0.5 mL of deionized water was added to the mixture, which was then transferred into a 120 mL flask. The glass bottle was sealed with aluminum foil pierced with four small holes and placed inside a desiccator with CO_2 atomsphere under 30 °C. The incubation lasted 36 h. The precipitate was purified by 50 % anhydrous ethanol and recovered by centrifugation, which was repeated for three times. Moisture was removed by incubating at 37 °C for 1 d. Morphology and elemental distribution of the $CaCO_3$@Nar nanoparticles were analyzed using TEM. The loading rate of Nar in the $CaCO_3$@Nar nanoparticles was measured using UV–vis spectroscopy. XPS was employed to analyze the ratio of Ca and C elements within the $CaCO_3$@Nar nanoparticles. Size distribution and charge status of $CaCO_3$@Nar nanoparticles were measured using nanoparticle size and zeta potential analyzer.

2.4. Preparation and characterization of EXO-H

HUVECs were cultured in high glucose DMEM supplemented with 10 % fetal bovine serum, 1 % penicillin, and 1 % streptomycin. The incubation condition was 37 °C and 5 % CO_2. When the cells reached approximately 20 culture flasks during normal passage, cells were transferred to serum-free DMEM and sealed with sterile membranes. The hypoxic incubation lasted another 48 h. Based on previous studies, we extracted exosomes using an ultra-high speed centrifuge, which were first centrifuged at 10,000 g for 30 min to decant the supernatant and then 120,000 g for 70 min twice for enriching EXO-H [16]. The isolated EXO-H were dispersed in PBS and placed in a −80 °C refrigerator. The concentration of exosomes was determined using a Pierce BCA Protein Assay Kit (Beyotime). Nanoscale morphology and elemental distribution of EXO-H derived from HUVECs were examined using TEM. The average particle size of the EXO-H was measured using nanoparticle size and zeta potential analyzer. Co-culture experiments were carried out by labeling EXO-H with DiI and incubating with HUVECs for 24 h, followed by CLSM to assess cellular uptake of EXO-H. EXO-H treated HUVECs were treated by trizol reagent to isolate the total RNA. RNA quality and associated genes were assessed on a StepOne RT-PCR System (Applied Biosystems) and the calculation was done via comparative Ct (ΔΔCt) method using GAPDH as standard.

2.5. Fabrication of layered MN patch

The SA solution was prepared by dispersing 2 g of SA in 100 mL of ddH_2O and stirring homogeneously for 48 h until it became clear. Meanwhile, type A gelatin (10 g) was dissolved in 100 mL ddH_2O at 55 °C with stirring with 1 mL of MA. Subsequently, samples were purified by dialysis at 55 °C for 3 d and recovered by lyophilization. Precursor solution for the top layer was prepared by adding $CaCO_3$@Nar nanoparticles to a 2 % SA solution and mixed thoroughly. Similarly, precursor solution for the bottom layer was prepared by adding EXO-H to a 20 % GelMA solution and well mixed. 2 mL SCa solution was added to the PDMS mold, vacuum pressure was applied in a vacuum drying chamber at room temperature to remove air bubbles, and the process was repeated 5 times. The mold was heated at 37 °C for at least 12 h, then added with GE solution. This treatment was repeated and then demolded to obtain the layered MNs.

2.6. Characterization of layered MN patch

The prepared SCa MN, GE MN, and SCaGE MN were cut into a shape of 10 × 10 array. After sputter-coating with gold for 30 s, the MNs were monitored under SEM and images were captured from multiple angles to examine their morphology. An appropriate amount of Rhodamine B dye was mixed with the SCa solution and FITC with the GE solution to prepare stained SCa MN, GE MN, and SCaGE MN, respectively. The prepared MNs were cut into a 10 × 10 array, and delamination of the MN was observed under CLSM.

The compression performance of SCa MN, GE MN, and SCaGE MN was tested using an IBTC-300 miniature multi-scale in-situ mechanical testing system. Changes in the compression force was measured using a 300 N sensor. The compression speed was 0.01 mm/s and measured compression distance were 0.8 mm.

MNs were immersed in 5 mL PBS (pH 7.4) and incubated at 37 °C for 24 h until they reached swelling equilibrium. Subsequently, the excess surface water was absorbed using filter paper, and the weight of the wet samples was recorded. The wet samples were subsequently dried at 37 °C until completely desiccated for weight measurement.

To assess degradation, MN patches were weighted and incubated in 5 mL PBS (pH = 7.4) at 37 °C. Certain samples were collected at day 0, 1, 4, 7, and 14, followed by centrifugation at 1000 rpm and drying at 37 °C for 24 h for weight measurement.

2.7. In vitro Nar release and antioxidant assay

$CaCO_3$@Nar and SCaGE MNs were immersed separately in PBS solutions at pH 4.5 and 7.4. At various time points, incubation solutions from different pH conditions were collected, and the concentration of Nar in the incubation solution was measured by profiling the light absorption at 301 nm.

DPPH working solution (0.2 mM) was obtained by mixing 2 mL of 95 % ethanol with 2 mL of DPPH stock solution. Subsequently, 2 mL of $CaCO_3$@Nar solution and Nar solution at the same concentration were separately mixed with 2 mL of the DPPH working solution. After thorough mixing, the mixture was placed in a dark room at ambient temperature for 30 min. Subsequently, its UV–vis absorbance was recorded at a wavelength of 517 nm.

2.8. In vivo skin treatment test

The fabricated layered MN patches were adhered onto the rat dorsal skin, where they were pressed for 10 s and 30 s. The skin samples were then observed using SEM to examine the morphology before and after MN insertion. SCaGE MNs were stained with FITC and applied to the dorsal skin of SD rats. After 30 s of mild pressing to maintain MN adhesion, the skin was extracted, and skin retention of MN was analyzed by performing layer-by-layer scanning of the skin samples using CLSM.

2.9. Biocompatibility

CCK-8 assay and Calcein-AM/PI live/dead cell dual staining kit were used to determine the impact of the patches on cell viability. Each microneedle group was irradiated with UV for 12 h, transferred to a 6-well plate, and an appropriate amount of serum-free medium was added to each well, incubated at 37 °C for 24 h. The supernatant was transferred to a centrifuge tube, centrifuged at 1200 rpm for 5 min, and the supernatant was collected and set aside. Approximately 1.2×10^4 HUVECs were seeded in 96-well plates with 100 μL of extract liquid per well. HUVECs were incubated at 37 °C for 1 and 3 d, and each experiment was conducted with five replicates per group.

2.10. Cell migration experiment

HUVECs were inoculated at 2×10^5 cells/well into 6-well plates. When cell confluence reached approximately 80 %, a scratching wound was created in the cell layer using a 200 μL pipette tip. Subsequently, cell debris and floating cells were removed by washing with sterile PBS thrice. Extracted solutions from SCa MN, GE MN, and SCaGE MN were diluted with PBS for treating the HUVECs. At 0, 12, and 24 h post-treatment, the wells were examined under a microscope to measure the width of the scratches. Photographs were taken to monitor the scratch closure over time. Cell migration ratio was calculated as the following equation:

$$\text{Migration ratio } (\%) = \frac{A1 - A2}{A1} \times 100\%$$

Here A1 represents cell coverage at 0 h, A2 represents the cell-covered area at designated time points.

2.11. Treatment-induced tube formation of endothelial cells

HUVECs were inoculated in 12-well plates at 1×10^5 cells/well. Prior to the experiment, serum-free medium was used for hypoxic culture of HUVECs. Matrigel matrix gel was thawed from −20 °C by placing it at 4 °C until fully melted. Once the Matrigel had melted, PBS and the extracted solutions from SCa MN, GE MN, and SCaGE MN were diluted 1:1 with the Matrigel matrix gel. Using pre-cooled tips, 50 μL of the diluted mixture was poured into 96-well plates of 37 °C and incubated for 1 h to enable Matrigel formation. HUVECs were seeded onto the solidified Matrigel at an appropriate cell density and incubated for 6 h. The cultured cell samples were monitored and imaged by an inverted optical microscope. Vascularization was quantitatively analyzed using ImageJ software.

2.12. Antioxidant efficiency of $CaCO_3$@Nar

The cellular ROS levels in HUVECs were detected using the fluorescent probe DCFH-DA. HUVECs were inoculated in 48-well plates at 5×10^4 cells/well. After PBS purification, the extracted solutions from SCa MN, GE MN, and SCaGE MN and different concentrations of $CaCO_3$@Nar mixture were added into the wells for 24 h incubation, followed by the addition 500 μM H_2O_2 solution for 4 h incubation, and again purified thrice by PBS. Appropriate volume of DCFH-DA working solution (10 μmol/L) was used to stain the cells for 20 min, followed by PBS washing thrice. The processed samples were measured by a fluorescence microplate reader to determine fluorescence intensity at 525 nm. Some of the samples were imaged by an inverted fluorescence microscope. A proportion of the samples were treated with 4 % paraformaldehyde for 30 min, purified thrice with PBS, and stain with DAPI to visualize the cell nuclei. Some of the PBS-washed samples were treated by anti-fade mounting medium to prevent fluorescence quenching. CLSM and ImageJ software were used to analyze cell morphology and fluorescence intensity.

2.13. Polarization status of macrophages

Raw264.7 cells were first inoculated in confocal dishes and then stimulated by LPS (1 μg/mL, 24 h), washed by PBS and then incubated by extracted solutions from SCa MNs, GE MNs, or SCaGE MNs for 48 h. The treated samples were fixed with 4 % paraformaldehyde for 30 min and then TBS-T purification thrice. 0.5 % Triton X-100 was used to permeabilized the cell for 15 min and again washed three times by TBS-T. Next, samples were first incubated with 5 % skim milk for 1 h. Primary antibodies against CD86 (1:200) or CD206 (1:200) were added and incubated overnight at 4 °C, again washed thrice by TBS-T, and then incubated with the fluorescent secondary antibodies for 60 min, purified thrice by TBS-T, stained by DAPI for 10 min, followed by another three rounds of TBS-T washing. CLSM was used to observe cell morphology, and fluorescence intensity was quantitatively analyzed using Image-J.

2.14. Flow cytometry test

RAW264.7 cells were inoculated into 6-well plates at a density of 2×10^5 cells/well and stimulated with LPS (1 μg/mL) for 24 h. After co-culturing with the addition of SCa, GE, and SCaGE leach solutions for 48 h, the well plates were washed with PBS, and the cells were digested with trypsin in EP tubes and centrifuged at 2000 rpm to remove the supernatant. The cells were resuspended in PBS and centrifuged at 2000 rpm to remove the supernatant. Fluorescent dyes (CD86:FITC and CD206:APC) were added after dilution with PBS (1:200) and incubated at room temperature for 30 min. The supernatant was removed by centrifugation at 2000 rpm, and the cells were resuspended in 200 μL of PBS. Fluorescence intensity was measured using flow cytometry (FACSVerse, BD, MSA), and data analysis was performed using FlowJo_v10.8.1.

2.15. ELISA test

Raw264.7 cells were inoculated in 24-well plates at a density of 5×10^5 cells/well and incubated with different MN extracts, $CaCO_3$@Nar, or EXO-H for 1 and 3 d. Supernatants were collected, and ELISA assays were performed. The OD values at 450 nm was measured accordingly.

2.16. Western blot (WB) test

Fibroblasts (NIH-3T3) were harvested and lysed by adding RIPA lysate containing PMDF (PMDF:RIPA = 1:100) for 10 min, then the cells were scraped off with a pipette tip, transferred to a 1.5 mL EP tube, centrifuged at 12000 rpm for 5 min, and then the supernatant was transferred to a new 1.5 mL EP tube. The extracted proteins were quantified using a BCA protein assay kit (Beyotime, China). The corresponding loading buffer was added to the protein solution, and a boiling water bath was applied for 10 min to completely denature the proteins, which were then used for electrophoresis (separation voltage, 120 V). Proteins were transferred to a PVDF membrane with 1 × transfer buffer (Servicebio, China) at 0.3 A for 90 min. Proteins were bound to a protein-free containment solution (Servicebio, China). The proteins were bound to a protein-free containment solution (Servicebio, China) for 2 h. The membrane was washed three times with TBST for 5 min each. The PVDF membrane was incubated with the corresponding primary antibody working solution (α-SMA polyclonal antibody, 1:1000, AF1032, Affinity, Australia) overnight and washed three times with TBST for 5 min each. The corresponding HRP-labeled secondary antibody working solution was added to the PVDF membrane and incubated for 1 h at room temperature, and the membrane was washed three times with TBST for 5 min each. The corresponding HRP-labeled secondary antibody working solution was added to the PVDF membrane and incubated for 1 h at room temperature, and the membrane was washed three times with TBST for 5 min each time. The developing solution was then added, photographed, and recorded using a developing instrument. After completion of the western chemiluminescence assay, the membrane was rinsed in distilled water for 5 min. Distilled water was discarded and an appropriate amount of Western Primary and Secondary Antibody Removal Solution (strong alkaline, Beyotime) was added to cover the membrane completely. Samples were rinsed for 5 min on an orbital shaker. Western primary and secondary antibody removal solutions were discarded and samples were rinsed twice with distilled water. Subsequent Western blotting procedures, such as blocking, were performed, and protein expression was analyzed quantitatively using ImageJ.

2.17. Burn wound grading test

SD rats were anesthetized by intraperitoneal injection of pentobarbital sodium, and hair removal creams were used to remove hair from the backs of the rats. Brass molds were heated to 200 °C, 300 °C, 400 °C, and 500 °C. The heated molds were then applied vertically to the back of the SD rats for 10 s without additional pressure to create a metal burn wound area of 1 cm × 1 cm. The rats were then euthanized to extract the burn wound and peripheral skin tissues, which were fixed with 4 % paraformaldehyde and analyzed after H&E staining.

2.18. In vivo wound healing

After intraperitoneal anesthesia and hair removal, brass molds were heated to 400 °C and applied vertically to the back of SD rats without additional vertical force for 10 s to create a 1 cm × 1 cm metal burn wound. SCa MN, GE MN, and SCaGE MN were then placed on the burn wound area and pressed vertically for 30 s before removing any excess material. The Control group received no treatment. Post-surgery, all rats were injected intraperitoneally with 40,000 units of penicillin daily for 7 d. Wounds were imaged on day 0, 4, 7, 14 and 21 after operation to observe the healing of the wound, and the change of wound size was statistically analyzed. The whole skin tissue around the wound was collected on the 7th, 14th and 21st day after surgery and fixed with paraformaldehyde. H&E staining and Masson's trichrome staining were used to analyze the histological details. Immunohistochemistry (IHC) staining for CD86, CD206, α-SMA, and CD31 was performed on wound tissues to evaluate inflammation status and neovascularization levels. Quantitative analysis of the fluorescence data was done with Image-J.

2.19. Statistical analysis

Data analyses were done by Origin 2021 and expressed as mean ± standard deviation (mean ± SD). Unpaired *t*-test was used for comparison between two groups and one-way analysis of variance for comparison between multiple groups. Statistical threshold was set to $P < 0.05$.

3. Results and discussion

3.1. Preparation of $CaCO_3$@Nar NPs

Herein, Nar molecules were loaded into $CaCO_3$ nanoparticles via a gas-diffusion-dependent approach [17], allowing the homogenous and efficient integration of the anti-inflammatory agents into the bio-responsive $CaCO_3$ nanoparticles substrates in a non-invasive fashion. To optimize the $CaCO_3$ NPs synthesis protocols for improving nanoproduct quality and Nar loading capacity, we have further investigated the nanoparticle morphology and composition using graded Nar to $CaCl_2$ ratios to determine the optimal synthesis conditions. According to TEM imaging and UV–vis spectroscopic analysis, the maximum ratio of Nar to $CaCl_2$ ratio was 1:1, beyond which no nanoparticles with regular shapes could be formed, and the loading efficiency of Nar was determined at 6.84 % with a final loading ratio of 11.41 % (Fig. S1 ABC). This is used as the standard condition for nanoparticle synthesis in the subsequent experiments. Notably, under the Nar:$CaCl_2$ feeding ratio of 1:1, the as-prepared $CaCO_3$@Nar NPs showed homogeneous spherical morphology (Fig. 2A–B). X-ray photoelectron spectroscopy (XPS) revealed that $CaCO_3$ samples have a Ca to C ratio of 25.6 %, whereas the Ca to C ratio in $CaCO_3$@Nar decreased to 15.6 %, attributing to the incorporation of Nar contents (Fig. 2C–D). Dynamic light scattering (DLS) tests in Fig. 2E revealed that the average size of pristine $CaCO_3$ NPs was in the range from 400 nm to 700 nm, which increased slightly to 700 nm–1000 nm for $CaCO_3$@Nar NPs. Zeta potential measurement results (Fig. 2F) showed that $CaCO_3$ exhibits a slightly negative surface charge (−3.16 mV), which switched to slightly positive for $CaCO_3$@Nar (1.31 mV) due to the characteristic positively charged status of Nar (6.93 mV). The results of DPPH assay on the antioxidant capacity of the samples in Fig. 2H showed that $CaCO_3$@Nar has similar antioxidant function like Nar, again validating the drug delivery capability of $CaCO_3$@Nar NPs.

3.2. Characterization of EXO-H

To obtain the EXO-H contents, HUVECs were incubated in hypoxic environment for 48 h, and the conditioned media were subjected to ultracentrifugation to isolate EXO-H. TEM and DLS analysis results (Fig. 3A–B and Fig. S1I) revealed that the diameter of EXO-H was in the range of 100 nm–150 nm, which were composed to typical elements including C, O, N, P, S, etc. Previous studies already confirmed that hypoxia conditioning has profound impact on the composition of exosome contents, particularly those angiogenesis-related factors including VEGF, TGF-β, HIF-1α, H19, and EFNA3 [18–22]. These factors can enhance the motility and vitality of endothelial cells to promote local angiogenesis. The pro-angiogenesis activity of EXO-H was further analyzed via real-time quantitative polymerase chain reaction (RT-qPCR) assay (Table S1). Compared with exosomes obtained under normoxic conditions (EXO-N), EXO-H treatment substantially enhance VEGF, TGF-β, HIF-1α, and H19 expression while suppressing EFNA3 expression in HUVECs (Fig. 3C–G), indicating that EXO-H can promote angiogenesis through influencing multiple pathways. As EXO-H needs to enter cells to exert its effects, to assess the uptake efficiency of EXO-H by HUVECs, EXO-H was labeled with DiI red fluorescent dye and co-cultured with HUVECs for 24 h before analysis by confocal laser

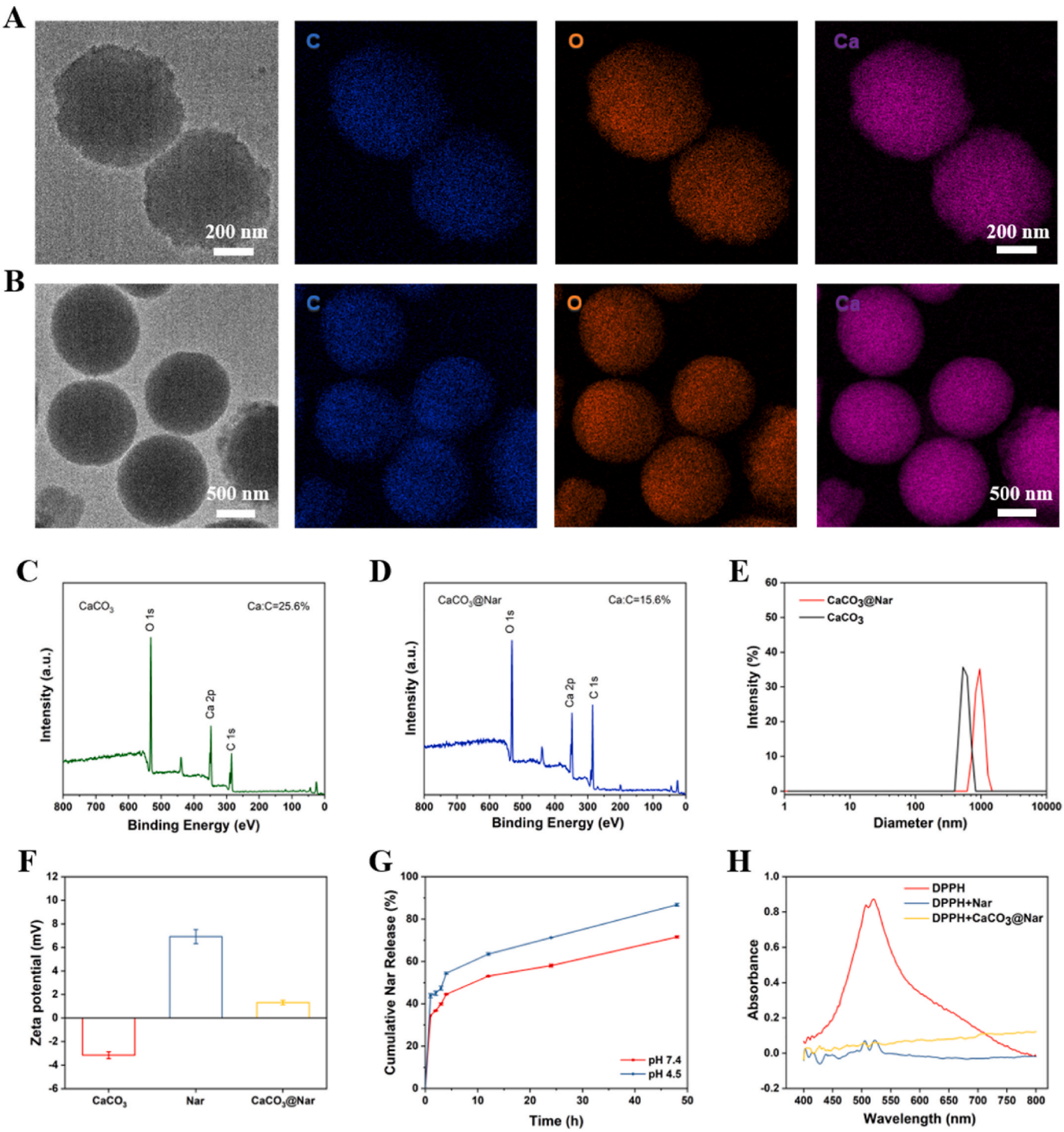

Fig. 2. (A) The TEM images of $CaCO_3$ NPs. (B) The TEM images of $CaCO_3$@Nar NPs. (C) The ratio of Ca and C in the $CaCO_3$ NPs. (D) The ratio of Ca and C in the $CaCO_3$@Nar NPs. (E) The particle size distribution of $CaCO_3$ NPs and $CaCO_3$@Nar NPs. (F) The zeta potentials of nanoparticles. (G) Cumulative drug release rate of $CaCO_3$@Nar NPs at different pH conditions. (H) ROS scavenging effect of Nar and $CaCO_3$@Nar NPs in vitro.

scanning microscopy (CLSM) [23]. The results demonstrated the successful uptake of EXO-H by HUVECs (Fig. 3H).

3.3. Characterization of functionalized layered MN patch

In this study, biocompatible SA and GelMA hydrogels were selected as the top and bottom materials of the MN for the incorporation of $CaCO_3$@Nar and EXO-H, respectively. These MNs were fabricated using a negative pressure molding and drying method. In this process, the precursor solution was first filled into the MN template under negative pressure to remove air bubbles and then dried at 37 °C for 12 h before demolding. As shown in Fig. 4A, the MN patch was of a square shape with 400 μm in width and 800 μm in height, while the microneedle density was 20 × 20. SA and GelMA have significant differences in mechanical properties. Indeed, SEM analysis of the MN morphology revealed distinct characteristics: the top layer prepared with a 2 % SA

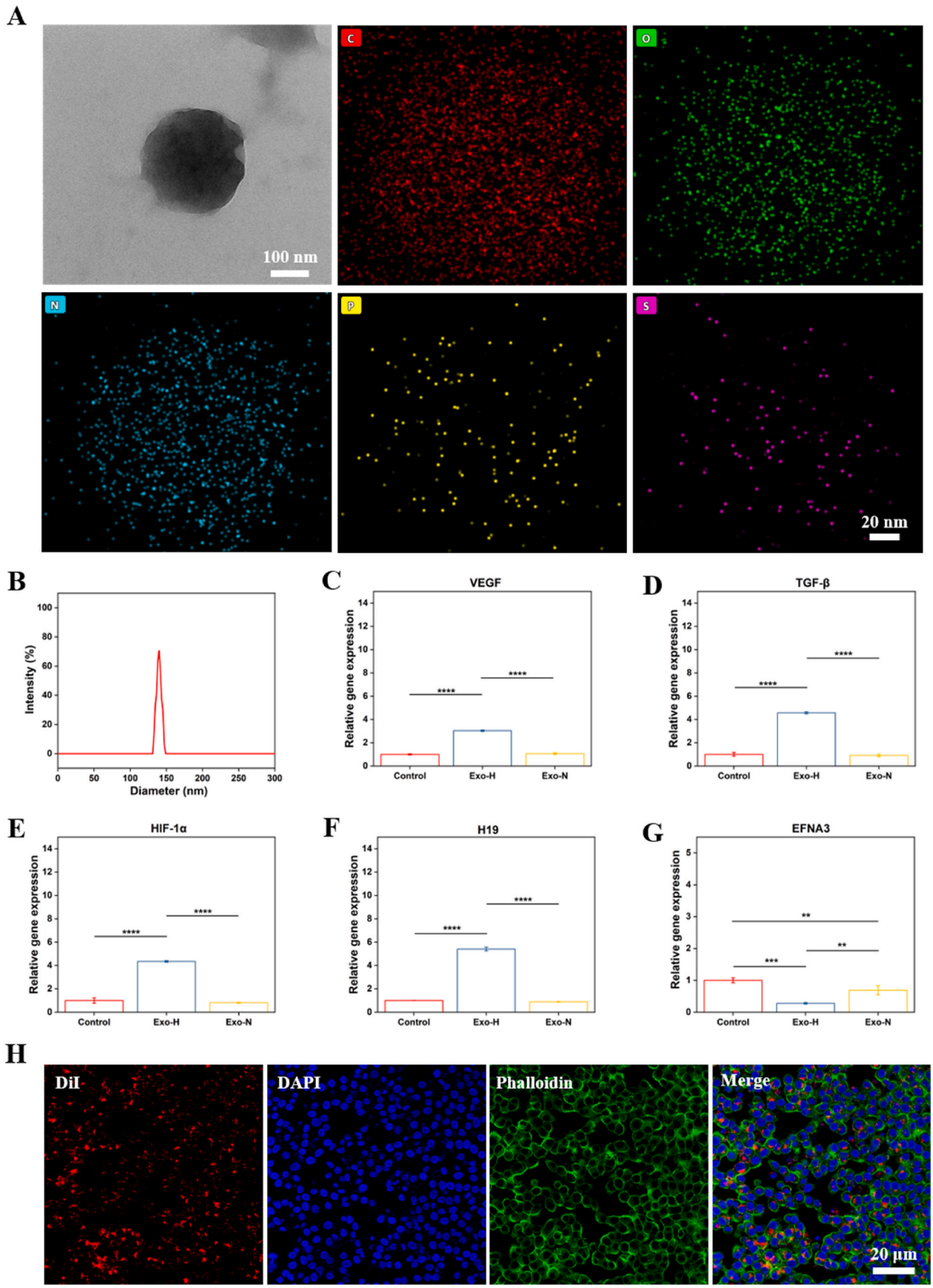

Fig. 3. (A) The TEM images of EXO-H. (B) The particle size distribution of EXO-H. (C) Relative gene expression of VEGF. (D) Relative gene expression of TGF-β. (E) Relative gene expression of HIF-1α. (F) Relative gene expression of H19. (G) Relative gene expression of EFNA3. (H) The CLSM image of DiI-labeled exosome uptake by HUVECs.

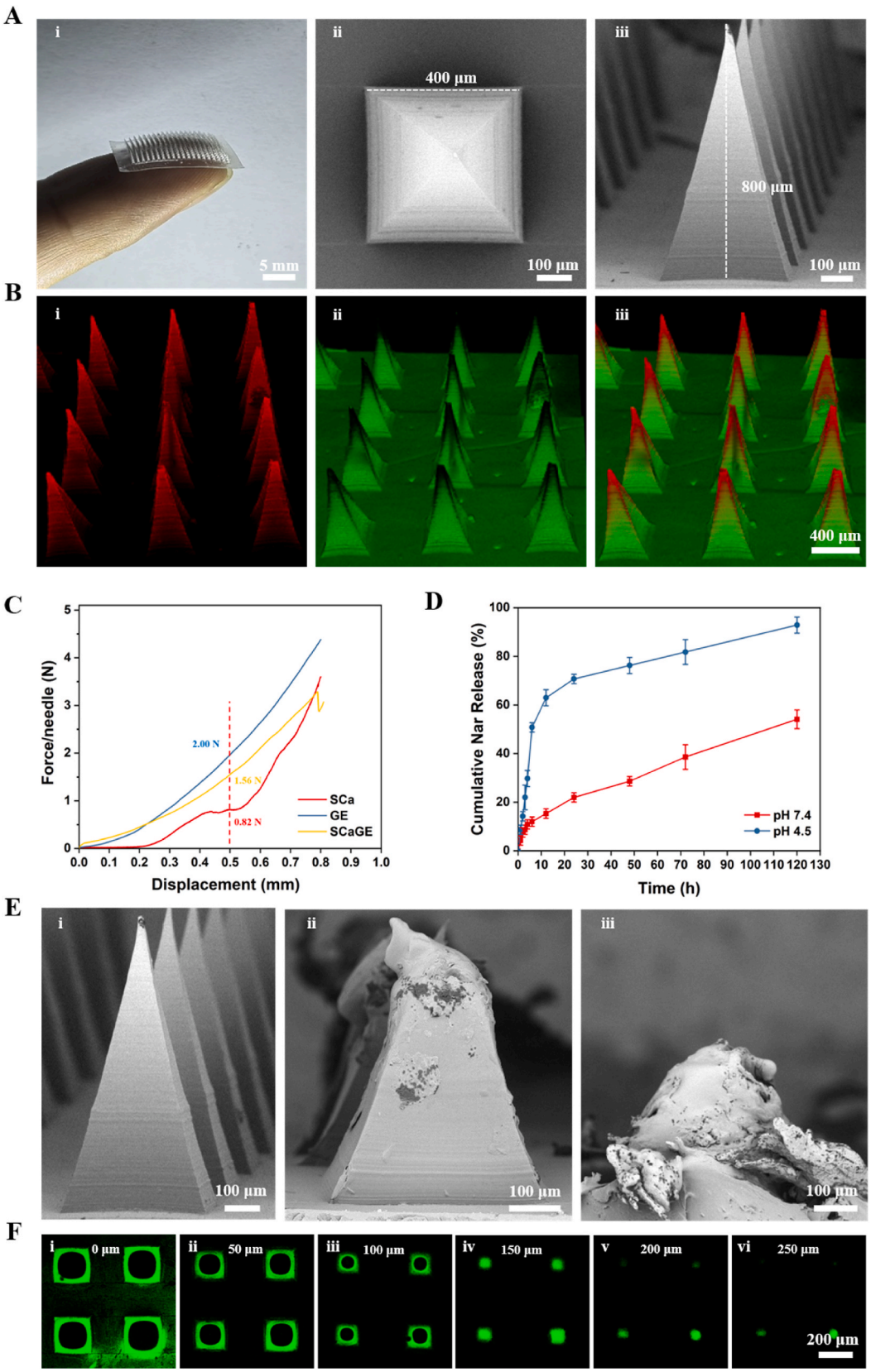

Fig. 4. (A) Morphology and size of MN. (i) Optical image of MN patch; (ii) SEM image showing the dimension of a single MN; (iii) SEM image showing the height of MN. (B) CLSM image of stained MN. (i) SCa MN; (ii) GE MN; (iii) SCaGE MN. (C) Mechanical strength of MN. (D) Cumulative drug release rate of layered MN at different pH conditions. (E) SEM images of MN punctured into the skin at different times. (i) 0 s; (ii) 10 s; (iii) 30 s. (F) CLSM images of the depth of SCaGE MN penetration into the skin after 30 s.

solution exhibited a shriveled and contracted appearance after demolding, indicating weaker mechanical properties (Fig. S1D i); the bottom layer prepared with a 20 % GelMA solution exhibited complete needle shapes with good mechanical properties after demolding (Fig. S1D ii); the layered MN fabricated using secondary vacuum negative pressure demolding exhibited intact needle shapes with improved mechanical properties, while retaining some characteristics of the SA layer (Fig. S1D iii). The layered structure of the MN patches was consistently supported by SEM analysis (Fig. S1F) and CLSM using fluorescently stained samples (Fig. S1E and Fig. 4B).

The mechanical strength of MN needles significantly influences their penetration ability [24]. Therefore, the maximum fracture force that the layered MNs can withstand was evaluated. During testing, MNs were mounted horizontally and the tips were oriented towards a slowly approaching force sensor. Subsequently, force measurements were initiated upon sensor contact with the MN tip, with the sensor moving continuously by 800 μm. The results (Fig. 4C) indicated a plateau phase in the mechanical performance of SCa MNs between 0.45 mm and 0.55 mm from the needle tip, suggesting susceptibility to fracture at this position, leading to reduced mechanical performance. In contrast, GE MNs and SCaGE MNs with GelMA did not exhibit such a plateau phase, likely due to the lower toughness of dried SA compared to GelMA. Relative to the center of the mechanical plateau phase of SA (0.5 mm from the needle tip), the maximum tolerable force load of SCa MNs was 0.82 N/needle, while that for GE MNs and SCaGE MNs was 1.56 N/needle and 2.00 N/needle, respectively. These findings indicate that individual needle tips of layered MN possess the mechanical strength required for skin penetration [25].

Normal skin maintains a pH in the range of 4–6, which increases significantly to near neutral or slight alkaline levels in the range of 7–8 under burn wound conditions [26–29]. Therefore, we chose pH 7.4 and pH 4.5 as the drug release pH conditions to comprehensively study the drug release properties of the MNs. SCaGE MNs were immersed in PBS buffers of near neutral pH (7.4) and acidic pH (4.5) to evaluate the in vitro drug release behavior of Nar, which is realized by measuring Nar levels in the incubation solution at different time points (Fig. 4D). The results indicate that the release of Nar at pH 7.4 is significantly slower than that at pH 4.5. In acidic and neutral environments, the release rates of Nar reached 50.8 % and 12.0 % within 6 h, and 70.7 % and 22.0 % within 24 h, respectively, which is beneficial for preventing burst drug release while enabling sustained pro-healing activity. Excellent water absorption capability facilitates the rapid absorption of wound exudate, formation of a hydrogel network, and promotion of drug release [30]. After 24 h of incubation at pH 7.4, the swelling ratio of SCa MN was the highest, reaching 1736 %, whereas those of GE MN and SCaGE MN were approximately 364 % and 414 %, respectively (Fig. S1G). The in vitro degradation of MNs contributes to understanding the relationship between needle retention time in vivo and sustained drug release. By immersing SCa MN, GE MN, and SCaGE MN in PBS (pH 7.4) for 1, 4, 7, and 14 d, the in vitro degradation rates of the microneedles were assessed (Fig. S1H). SCa MN degraded by 54.2 % and 79.9 % at 4 and 14 d, respectively. In contrast, GE MN showed the fastest degradation rate, degrading by 72.1 % and 90.1 % at 4 and 14 d, respectively. SCaGE MN exhibited an intermediate degradation rate, degrading by 63.2 % and 86.2 % at 4 and 14 d, respectively. It is noteworthy that MNs rapidly absorbed water and fragmented into smaller pieces after immersion in PBS.

The morphological changes of SCaGE MNs before and after skin penetration were further analyzed (Fig. 4E). After 10 s of penetration, only the tip of the needle was dissolved while the overall structure remained intact; however, after 30 s, the majority of the needle body have been dissolved. This indicates that the MN structures could be efficiently dissolved by the interstitial fluid after entering skin tissues, thereby facilitating the delivery of functional contents deep into the burn wound. To further assess the SCaGE MN penetration performance into the skin, FITC-stained SCaGE MNs were administered onto the skin for 30 s and analyzed using CLSM to capture fluorescent images at different depths from the skin surface (Fig. 4F). The results show that the MN structures remain intact when the penetration depth was below 150 μm, beyond which the MNs have been dissolved. This is consistent with the dissolution state of MN depicted in Fig. 4E iii.

3.4. In vitro biocompatibility and functional analysis

To investigate the biocompatibility of MNs, HUVECs were treated by $CaCO_3$@Nar at various concentrations for 1 or 3 d, followed by cell viability assays using CCK-8 (Fig. S3C). After co-culturing for 1 d, cell viability in the treatment group was lower than blank control. However, after co-culturing for 3 d, this trend was reversed, showing that $CaCO_3$@Nar promoted cell proliferation in the dose range of 50–100 μg/mL. Therefore, concentration of $CaCO_3$@Nar was set to 100 μg/mL in subsequent experiments. The biocompatibility of the MNs was validated (Fig. 6C). After 1 d of co-culturing, the cell viability relative to the control group was 85.6 % and 87.4 % for the SCa MN and GE MN groups, whereas that for the SCaGE MN group reached 102.4 %. After 3 d of co-culturing, the cell viability of the SCa MN, GE MN, and SCaGE MN groups was 83.4 %, 80.2 % and 87.3 % of the control group.

SCa MN, GE MN, and SCaGE MN were co-cultured with HUVECs for 1 d and 3 d, followed by staining of live and dead cells using Calcein/PI cell viability assay kit. The viability of HUVECs was observed using inverted fluorescence microscopy (Fig. S3A) using live/dead staining. After 1 d of co-culture, exhibited slightly higher cell death rate than control, although the total amount of dead cells was still negligible. After 3 d of co-culture, cell death rate of SCa, GE and SCaGE groups remained at a similar level to control, supporting the cytocompatibility of the layered MNs.

Macrophages are critical mediators of inflammatory reaction in burn wound site through leveraging the cytokine secretion levels [31]. These cytokines not only regulate the inflammatory response during the acute phase but also facilitate the clearance of damaged neutrophils in the later stages, thus driving the wound for the proliferative phase [32]. To investigate if the layered MNs could alter the macrophage phenotypes, they were used to treat LPS-stimulated Raw264.7 cells for 24 h, afterwards the expression of M1 macrophage-characteristic CD86 (red fluorescence) and M2 macrophage-characteristic CD206 (green fluorescence) was analyzed using CLSM to indicate their polarization state (Fig. 5A). LPS-stimulated Raw264.7 cells showed strong red fluorescence that was indicative of polarization towards the M1 phenotype. The red fluorescence intensity significantly decreased in the $CaCO_3$@Nar-loaded SCa MN and SCaGE MN groups with increasing green fluorescence, while the fluorescence intensity in the $CaCO_3$@Nar-free GE MN group did not show significant fluorescence changes (Fig. 5C–D). This indicates that $CaCO_3$@Nar in the SCa MN and SCaGE MN groups can repolarize M1 macrophages into M2 phenotype to reduce the M1/M2 macrophage ratio in the wound bed. The results of quantitative flow cytometry analysis were consistent with the results of CLSM, where the SCa, GE, and SCaGE groups had a 23.69 %, 15.93 %, and 38.36 % decrease in CD86 expression levels and a 4400.00 %, 2755.26 %, and 5163.15 % increase in CD206 expression compared to the LPS + group (Fig. S6).

The secretion levels of IL-6, TNF-α and IL-10 were analyzed using ELISA. First, the anti-inflammatory effects of $CaCO_3$@Nar and EXO-H were analyzed (Figs. S2C–E). Both $CaCO_3$@Nar nanoparticles and EXO-H demonstrated anti-inflammatory capabilities, and $CaCO_3$@Nar was identified as the primary contributor for the anti-inflammatory effects. Subsequently, we studied the impact of various treatments on the secretion of IL-6, TNF-α and IL-10 by LPS-stimulated Raw264.7 cells. ELISA test results in Fig. 5F–H revealed that SCa MN and SCaGE MN treatments substantially reduced IL-6 and TNF-α secretion compared with the LPS group and GE MN group while enhancing IL-10 secretion. These findings suggest that $CaCO_3$@Nar effectively repolarized LPS-stimulated Raw264.7 cells into an anti-inflammation phenotype.

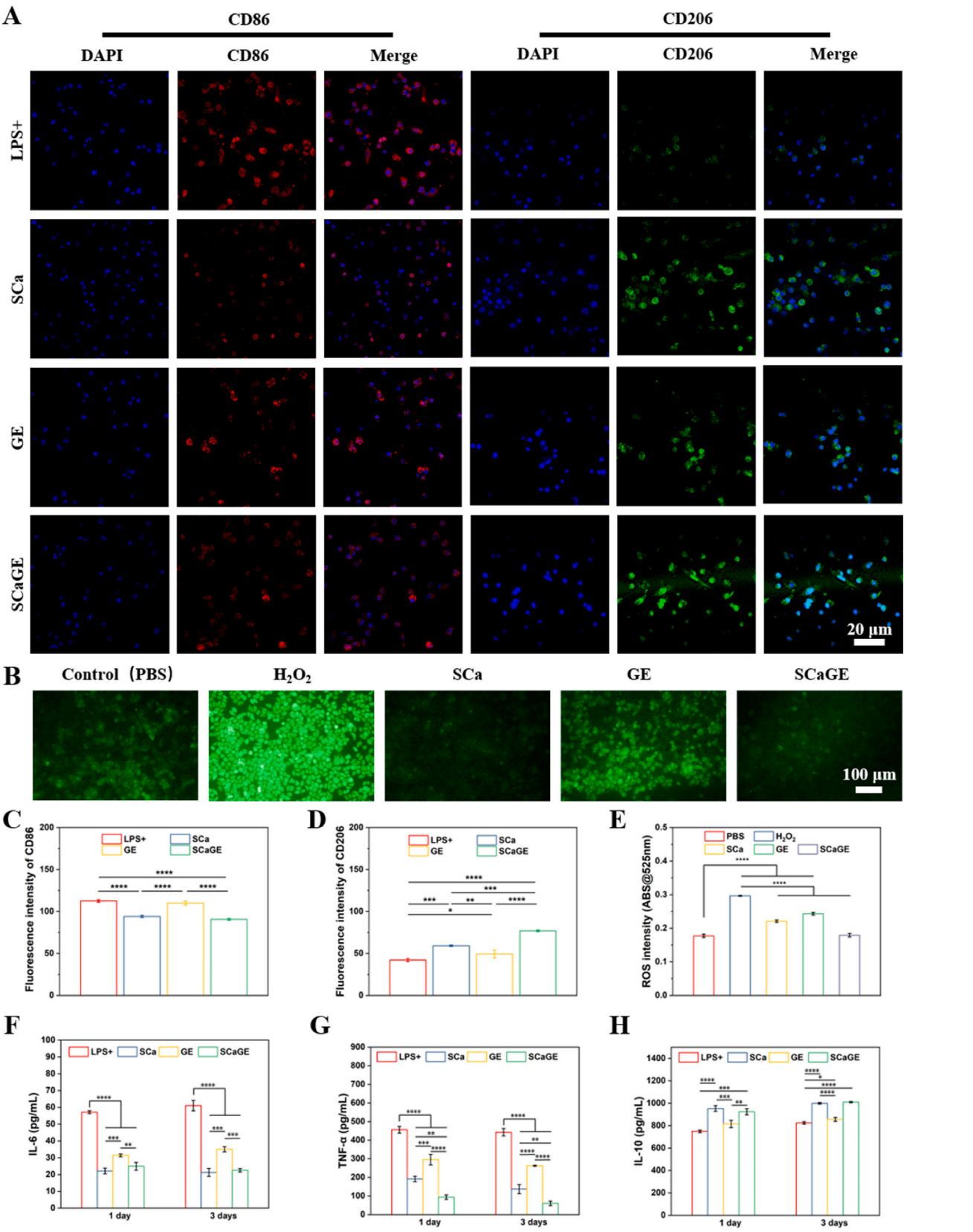

Fig. 5. (A) Immunofluorescence staining of the RAW264.7 cells. CD86 (red): M1 macrophages; CD206 (green): M2 macrophages; DAPI (blue): nuclei. (B) Fluorescence microscopy images of HUVECs using DCFH-DA as the fluorescent probe. (C) Immunofluorescence intensity of CD86. (D) Immunofluorescence intensity of CD206. (E) Statistical analysis of ROS intensity from fluorescence microscopy images. (F) ELISA assay of IL-6. (G) ELISA assay of TNF-α. (H) ELISA assay of IL-10. n = 3, *$p < 0.05$ and **$p < 0.01$.

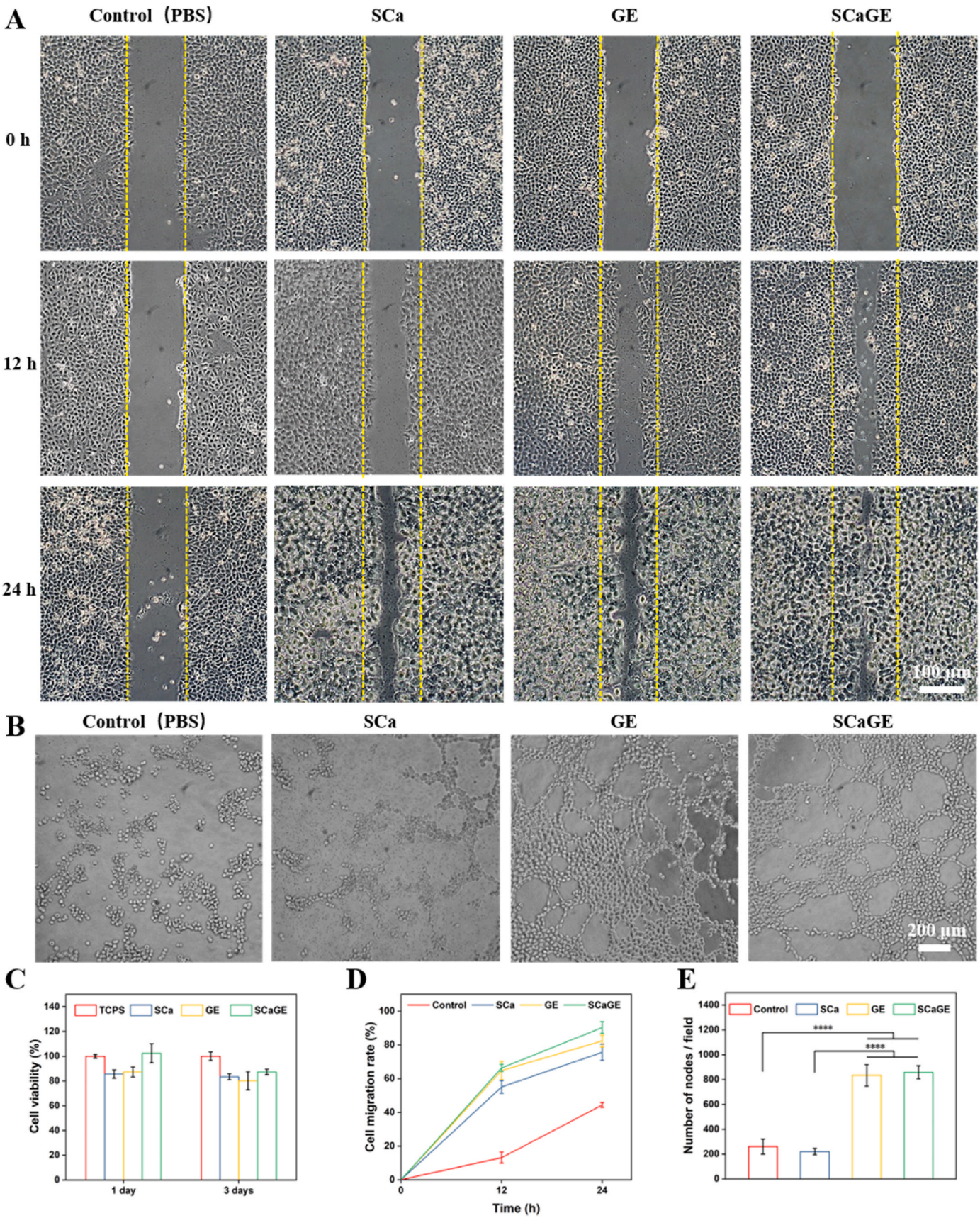

Fig. 6. (A) Scratch assay images of HUVECs cultivated in the medium supplemented with PBS (Control), SCa MN, GE MN or SCaGE MN. (B) Matrigel angiogenesis assay in HUVECs cultured in the medium supplemented with PBS (Control), SCa MN, GE MN or SCaGE MN. (C) The viability of HUVECs after incubation with MN for 1 d and 3 d. (D) Cell migration rate of HUVECs. (E) Matrigel angiogenesis assay in HUVECs. n = 3, *p < 0.05 and **p < 0.01.

Reactive oxygen species (ROS) are implicated in various stages of wound healing by influencing processes such as inflammation control, cell growth, angiogenesis, granulation tissue formation, and extracellular matrix synthesis. However, prolonged ROS stress can potentially delay or impair wound healing [33]. Nar exhibits excellent anti-inflammatory and ROS scavenging abilities, which have been confirmed through in vitro experiments. Indeed, $CaCO_3$@Nar showed potent ROS scavenging capabilities in a dose-dependent manner (Figs. S2A–B). SCa MN, GE MN, and SCaGE MN extracts were co-cultured with H_2O_2-prestimulated HUVECs for 24 h. DCFH was used to label intracellular reactive oxygen species (ROS), cell images were recorded and ROS fluorescence intensity was detected (Fig. 5B–E). Compared with the H_2O_2 group, SCa MN and SCaGE MN groups loaded with $CaCO_3$@Nar exhibited significant ROS scavenging effects, while the GE MN group showed a modest ROS scavenging ability. This indicates that $CaCO_3$@Nar effectively reduces ROS levels within HUVECs, demonstrating strong antioxidant capability.

Cell migration plays a critical role in angiogenesis and tissue remodeling [34]. To assess the influence of MNs on cell migration, scratching assays were carried out using HUVECs with SCa MN, GE MN, and SCaGE MN treatments for 12 h and 24 h. The cell scratch areas were photographed, recorded, and analyzed to calculate the migration rate (Fig. 6A–D). The SCaGE MN group exhibited the highest average migration rate at 24 h, reaching 90.3 ± 3.5 %, while the control group, SCa MN, and GE MN had average migration rates of 44.4 ± 1.5 %, 75.6 ± 4.8 %, and 82.4 ± 3.5 % at 24 h, respectively, supporting the potent capability of SCaGE MN to promote skin cell migration in the burn wound site to facilitate tissue regeneration.

Neovascularization is crucial for sustaining the nutrient supply to wound tissues and promoting scarless wound healing [35]. To study if EXO-H could enhance the angiogenesis capacity of endothelia cells, different concentrations of EXO-H were used to treat HUVECs on Matrigel for 6 h, and tube formation by HUVECs was observed using inverted microscopy. As shown in Figs. S3B and D, higher concentrations of EXO-H resulted in superior promotion of angiogenesis compared to the control group. It is also notable that the pro-angiogenesis efficacy of EXO-H reached a plateau when its concentration increased above 25 μg/mL. Therefore, EXO-H dose in the subsequent experiments was determined at 25 μg/mL. Further test of the MN-mediated tube formation effect (Fig. 6B–E) showed that GE MN and SCaGE MN loaded with EXO-H demonstrated significant promotion of angiogenesis than the other groups. However, tube formation by EXO-H-free SCa MN was similar to the control group. This indicates that EXO-H could stimulate the angiogenesis activity of endothelial cells. Interestingly, we also observed that the MN treatment was correlated with a low α-SMA expression level when the treatment was complete, which is a well-established indicator of low scar forming risks (Fig. 8E and Fig. S5).

3.5. Skin burn wound model and in vivo wound healing properties

Temperature and burn duration have significant impacts on skin injury. Following the analysis of statistical data related to burn models [13], a contact burn time of 10 s and a burn area of 1 cm^2 were selected. The severity of burns was assessed based on criteria including sebaceous gland disappearance, fibrous tissue proliferation, and inflammatory cell infiltration observed in H&E staining results [36]. Through statistical analysis of H&E staining results (Figs. S4A–B), a scoring system for assessing burn injury severity was developed (Table S2). The results indicate that normal tissues exhibit mild fibrous tissue proliferation and inflammatory cell infiltration, whereas skin tissues that were touched by hot metal rods show severe sebaceous gland disappearance, fibrous tissue proliferation, and inflammatory cell infiltration. Contact with metal rods of 200 °C, 300 °C, and 400 °C resulted in substantial damage to the dermis, demonstrating a positive correlation between burn severity and the temperature of the metal rod. A burn temperature of 500 °C results in severe damage to sebaceous glands and hair follicles, affecting the entire skin structure. To preserve the integrity of subcutaneous tissues, in vivo analyses in this study were all carried out under a metal rod temperature of 400 °C.

The efficacy of SCaGE MNs in treating thermal burn wounds was evaluated on thermal burn-bearing male Sprague-Dawley (SD) rats weighing approximately 300 g. Rats in different groups were treated by blank control, SCa MN, GE MN, and SCaGE MN. First, a custom brass mold was heated to 400 °C. The shaved dorsal skin of SD rats was then vertically exposed to this heated mold for 10 s to establish a high-temperature burn model. Subsequently, MN patches from the SCa MN group, GE MN group, and SCaGE MN group were pressed onto the surface of the burn wounds for 30 s. MN patches were applied again on day 0, 3, and 6 following the initial treatment. The wounds were imaged on day 0, 4, 7, 14, and 21 to assess the ability of the patches to promote wound healing (Fig. 7A). Results showed that within 4 d post-operation, the area of the burn skin wounds expanded, likely due to a reactive response of the surrounding skin tissues to the injury at the burn site. Subsequently, scabbing began at the wound site, and as healing progressed, the scabs gradually fell off, leading to a reduction in total wound area. Compared to the blank group, the SCaGE MN group exhibited the fastest wound closure, with scabs completely falling off by day 7, while the blank group and SCa MN group still had partial scabbing at day 14. Moreover, from day 7 onward (Fig. 7C), rats in the SCaGE MN group showed faster healing rate than all the other groups.

To comprehensively assess the healing of burn wounds, skin tissue samples from the wound area were processed by H&E staining and Masson's trichrome staining (Fig. 7B) for microscopic observations. H&E staining revealed that at 7 d post-operation, samples from the control group remained severely damaged and the sebaceous glands and hair follicles were still in a compromised state, while scabs were tightly adhered to the wound tissues. In contrast, partial scabbing was observed in the SCa MN and GE MN groups, while the SCaGE MN group showed complete scab detachment, accompanied by infiltration of abundant inflammatory cells in the wound tissue. By day 14 post-operation (Fig. S4C), scabs in the blank group and SCa MN group were nearly completely detached, with slightly enhanced restoration of sebaceous glands and hair follicles in the SCa MN group compared to the blank group. Scabs were fully detached in the GE MN and SCaGE MN groups, and skin surface layers showed obvious signs of reconstruction, and the SCaGE MN group exhibited lower levels of inflammatory cell infiltration compared to the GE MN group, indicating superior repair outcomes. By the 21st day of treatment, new sebaceous glands had appeared at the wound sites of all experimental groups, and the epidermal and dermal layers were fully reconstructed in the GE MN and SCaGE MN groups, with almost complete restoration of skin structure. Analysis of Masson staining results revealed that from post-operative day 7 to day 21, GE MN and SCaGE MN groups presented greater collagen deposition than the other groups (Fig. 7D). At 7 d post-operation, collagen deposition in the GE MN and SCaGE MN groups with EXO-H was at similar levels, but by day 21 of treatment, SCaGE MN group showed more collagen deposition than GE MN group. Collagen fibers from the GE MN and SCaGE MN groups appeared denser and more mature, further demonstrating that EXO-H can enhance collagen deposition levels during later stages of wound repair.

The anti-inflammation efficacy of layered MNs on rat models was investigated by immunohistochemical staining of CD86 and CD206. Fig. 8A and B showed that on day 7 post treatment, blank group presented greater CD86 expression than the experimental groups, reaching a relative intensity of 19.3 ± 1.2 %. In contrast, relative CD86 expression in SCa MN group (7.19 ± 0.43 %) and SCaGE MN group (4.13 ± 0.13 %) was much lower, attributing to $CaCO_3$@Nar. This trend in CD86 levels was maintained to day 21. Statistical analysis on the CD206 positive area (Fig. 8C–D) showed that on day 7 post-operation, the SCa MN group loaded with $CaCO_3$@Nar exhibited the best anti-inflammatory effect (19.6 ± 0.55 %), while that for the blank group, GE MN group, and SCaGE MN group were still 12.9 ± 0.25 %, 14.3 ±

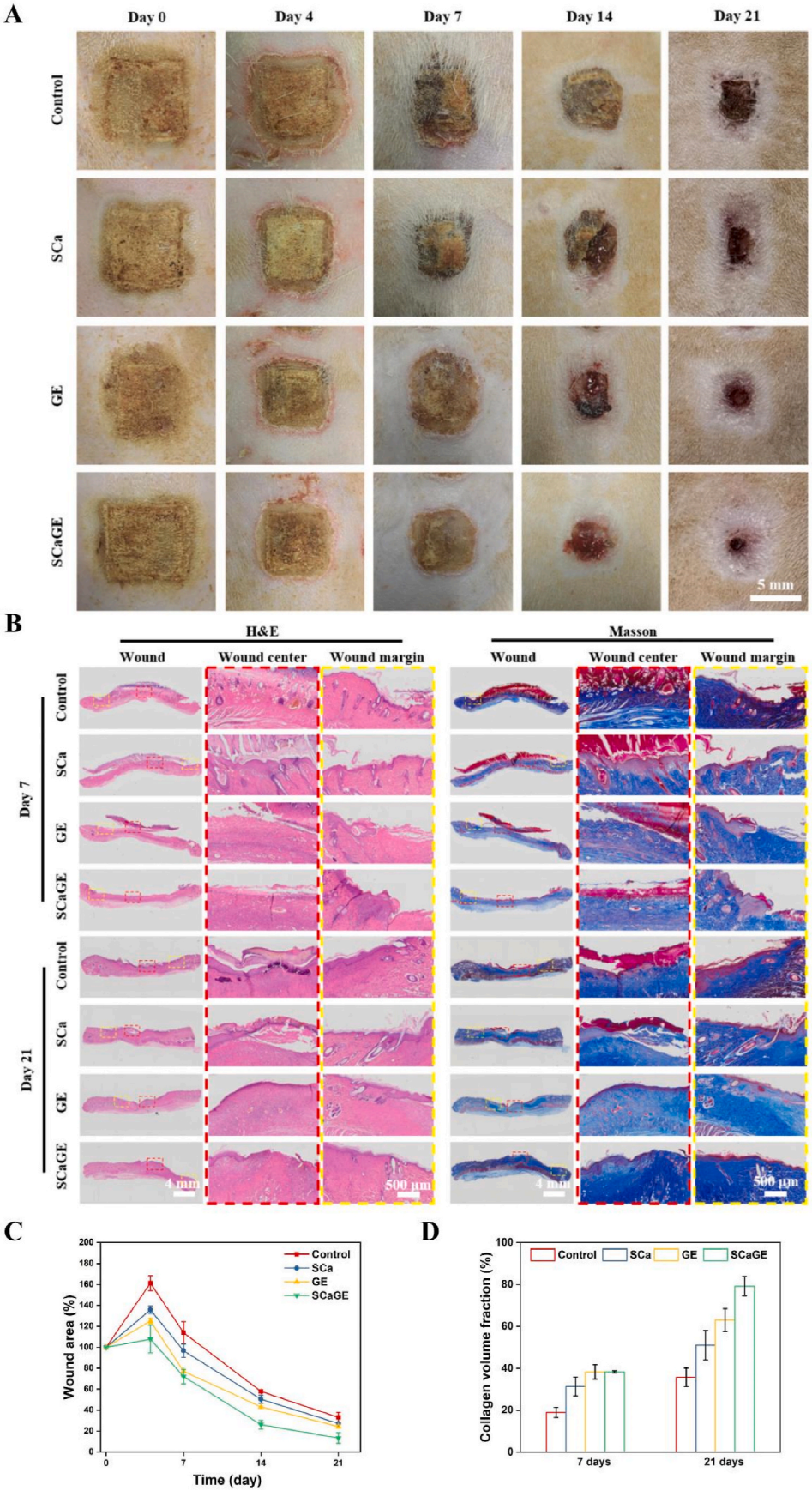

Fig. 7. (A) The photos of wound closure in different treatment groups on day 0, 4, 7, 14, and 21. (B) The H&E and Masson staining images of different treatment groups after operation for 7 d and 21 d. (C) The quantitative analysis of wound areas in different treatment groups. (D) Collagen volume fraction in different treatment groups on day 7 and 21.

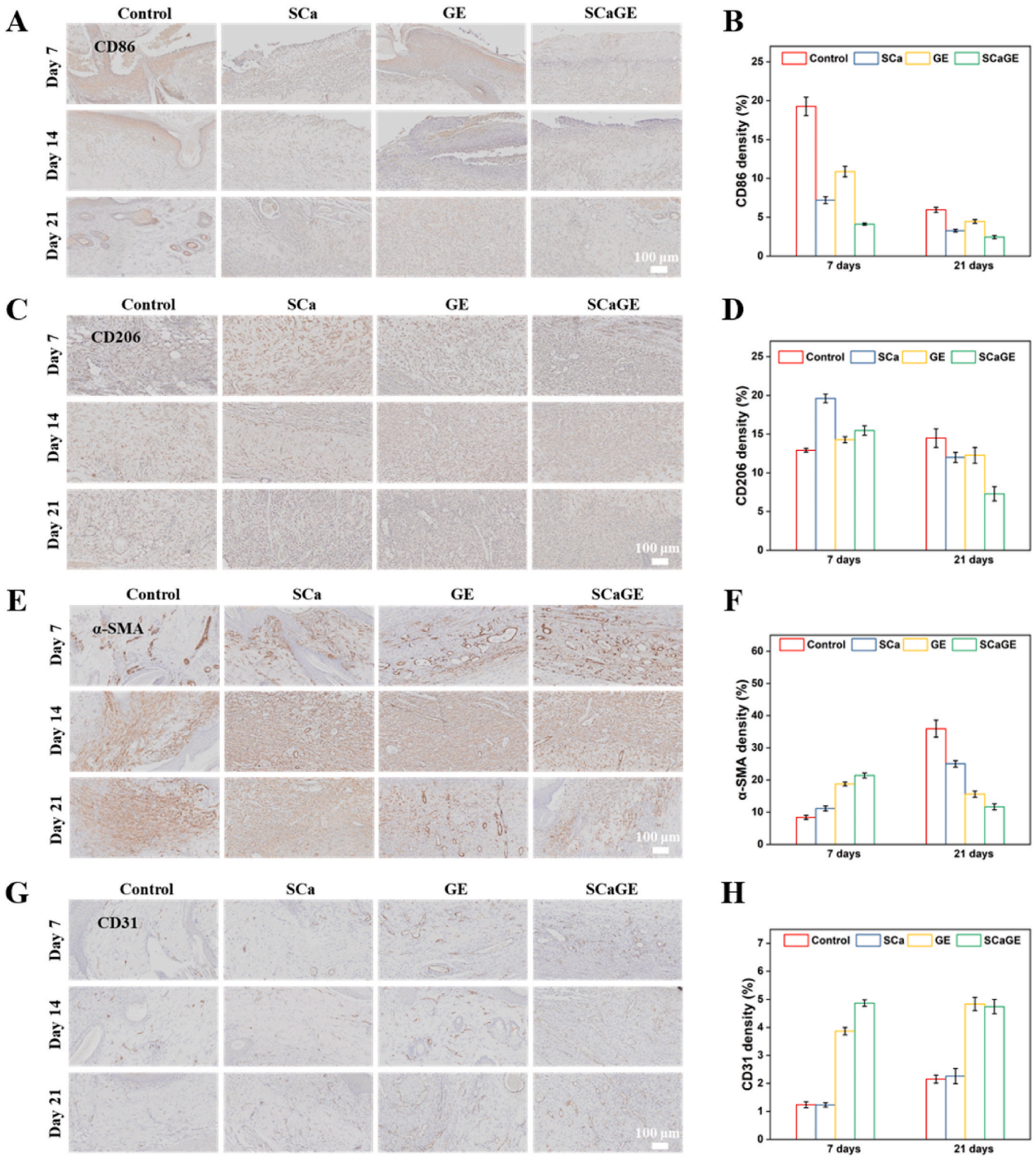

Fig. 8. The (A) CD86, (C) CD206, (E) α-SMA and (G) CD31 immunohistochemistry staining images of MN groups after operation for 7 d, 14 d and 21 d, respectively. The quantitative analysis of positive areas in (B) CD86, (D) CD206, (F) α-SMA and (H) CD31 immunohistochemistry staining images on day 7 and 21.

0.39 %, and 15.5 ± 0.62 %, respectively. However, in the later stages of wound repair, the blank group showed higher anti-inflammatory factor secretion than the experimental groups, possibly due to higher post-injury inflammation levels in the blank group that retards the repair process. To further substantiate our conclusions, flow cytometry was used to assess the proportion of M1-and M2-type macrophages in the tissue samples from individual groups, where the SCa, GE, and SCaGE groups had 9.75 %, 6.35 %, and 13.72 % decreases in CD86 fluorescence intensity and 501.23 %, 225.92 %, and 835.80 % increases in CD206 fluorescence intensity compared with the TCPS group (Fig. S7). These results indicate that $CaCO_3$@Nar loaded in the MNs can effectively confer anti-inflammatory effects during the initial stages of wound

healing.

Scarring event is closely related the generation of new blood vessels and tissue repair processes [37]. The effects of layered MNs on promoting angiogenesis and preventing scar formation in vivo was conducted using immunohistochemical staining for α-SMA and CD31. As shown in Fig. 8E and F, during the early phase of wound repair, the experimental groups presented more α-SMA positive area than the control group. The α-SMA intensities for SCa MN group, GE MN group, and SCaGE MN group were 11.1 ± 0.73 %, 18.8 ± 0.6 %, and 21.4 ± 0.79 %, respectively, whereas the α-SMA intensity in the blank group was 8.4 ± 0.63 %. This indicates that the experimental groups exhibited faster wound healing rates in the early stages. However, as the burn wound repair progressed into late stages, the α-SMA-positive area was higher in the blank group, with an α-SMA intensity of 35.9 ± 2.63 %, whereas the α-SMA intensities in the GE MN group and SCaGE MN group decreased to 15.6 ± 0.94 % and 11.6 ± 0.96 %, respectively. According to relevant studies, high expression of α-SMA during early wound healing significantly accelerates the secretion of extracellular matrix (ECM), thereby promoting wound closure. However, during late stages of wound healing, lower α-SMA expression levels are more preferable for reducing the risk of scar formation. This result is consistent with the results of in vitro cellular experiments (Fig. S5.). Additionally, immunohistochemical staining of CD31 was carried out to assess the formation of neovascularization (Fig. 8G–H) [38]. Both the GE MN group and SCaGE MN group exhibited the highest CD31-positive area throughout the repair process. Specifically, the relative ratios of CD31-positive areas were 3.9 ± 0.14 % and 4.9 ± 0.12 % on the 7th day after MN patch administration, and 4.8 ± 0.23 % and 4.7 ± 0.26 % on day 21 post-operation. This is primarily attributed to the EXO-H loaded in the core of the MNs, which effectively increased the level of vascularization in the wound area.

4. Conclusion

In summary, this study utilized layered MNs as carriers for the hierarchical integration of Nar and EXO-H for treating thermal burn wounds. The layered MNs enabled facile penetration of the burn-induced eschar to potentiate efficient delivery of Nar and EXO-H to the whole wound. The $CaCO_3$@Nar NPs in the top layers demonstrates excellent anti-inflammatory and ROS scavenging capabilities through the spontaneous Nar release after skin attachment. Meanwhile, the GelMA in the bottom layer provides sufficient mechanical strength to ensure MN penetration into the skin and facilitates rapid release of incorporated EXO-H to promote endothelial cell-dependent angiogenesis through stimulating multiple pathways. Additionally, the layered MNs demonstrate excellent biocompatibility and substantially promoted scarless burn wound healing in vivo, supporting its potential utility for burn wound treatment in the clinics.

CRediT authorship contribution statement

Hang Chen: Writing – original draft, Methodology, Investigation, Formal analysis, Data curation. **Lu Tan:** Writing – review & editing, Supervision, Conceptualization. **Liqi Li:** Writing – original draft, Investigation, Formal analysis, Data curation. **Yan Zheng:** Methodology, Investigation, Data curation. **Menghuan Li:** Writing – original draft, Supervision, Project administration. **Shuohan He:** Methodology, Investigation. **Zhong Luo:** Writing – review & editing, Supervision, Project administration, Funding acquisition. **Kaiyong Cai:** Supervision, Project administration, Funding acquisition. **Yan Hu:** Writing – review & editing, Validation, Supervision, Project administration, Funding acquisition.

Declaration of Competing Interest

The authors declare that they have no known competing financial interests or personal relationships that could have appeared to influence the work reported in this paper.

Acknowledgement

The authors would like to thank the Analytical and Testing Center of Chongqing University for their assistance during sample characterization. This study is financially supported by Natural Science Foundation of Chongqing Municipal Government (cstb2022nscq-msx0488), National Key Research and Development Program of China (2022YFB3804400), National Natural Science Foundation of China (11832008 and 92059107), Chongqing Graduate Scientific Research and Innovation Program (cYB20047, cYS20043), Chongqing Outstanding Young Talent Supporting Program (cstc2021ycjh-bgzxm0124), Natural Science Foundation of Chongqing (CSTB2023NSCQ-MSX0956), teaching research project of Army Medical University (2023B23), special project of improving scientific and technological innovation ability of Army Medical University (2023XJS35), and Xinqiao hospital Young Doctor Incubation Program (2022YQB033).

Appendix A. Supplementary data

Supplementary data to this article can be found online at https://doi.org/10.1016/j.mtbio.2024.101359.

Data availability

Data will be made available on request.

References

[1] C. Smolle, J. Cambiaso-Daniel, A.A. Forbes, P. Wurzer, G. Hundeshagen, L. K. Branski, F. Huss, L. Kamolz, Recent trends in burn epidemiology worldwide: a systematic review, Burns 43 (2017) 249–257.
[2] S. Amini-Nik, Y. Yousuf, M.G. Jeschke, Scar management in burn injuries using drug delivery and molecular signaling: current treatments and future directions, Adv. Drug Deliv. Rev. 123 (2018) 135–154.
[3] Y. Wang, J. Beekman, J. Hew, S. Jackson, A.C. Issler-Fisher, R. Parungao, S. S. Lajevardi, Z. Li, P.K.M. Maitz, Burn injury: challenges and advances in burn wound healing, infection, pain and scarring, Adv. Drug Deliv. Rev. 123 (2018) 3–17.
[4] K. Lu, K. Li, M. Zhang, Z. Fang, P. Wu, L. Feng, K. Deng, C. Yu, Y. Deng, Y. Xiao, P. Zhu, R. Guo, Adipose-derived stem cells (ADSCs) and platelet-rich plasma (PRP) loaded gelatin/silk fibroin hydrogels for improving healing in a murine pressure ulcer model, Chem. Eng. J. 424 (2021) 130429.
[5] J. Yang, W. Zeng, P. Xu, X. Fu, X. Yu, L. Chen, F. Leng, C. Yu, Z. Yang, Glucose-responsive multifunctional metal-organic drug-loaded hydrogel for diabetic wound healing, Acta Biomater. 140 (2022) 206–218.
[6] L.A. Elfawy, C.Y. Ng, I.N. Amirrah, Z. Mazlan, A.P.Y. Wen, N.I.M. Fadilah, M. Maarof, Y. Lokanathan, M.B. Fauzi, Sustainable approach of functional biomaterials-tissue engineering for skin burn treatment: a comprehensive review, Pharmaceut. Biol. 16 (2023) 701.
[7] G. Ma, C. Wu, Microneedle, bio-microneedle and bio-inspired microneedle: a review, J. Contr. Release 251 (2017) 11–23.
[8] Y. Wang, H. Lu, M. Guo, J. Chu, B. Gao, B. He, Personalized and programmable microneedle dressing for promoting wound healing, Adv. Healthc. Mater. 11 (2022) 2101659.
[9] Y. Su, A. McCarthy, S.L. Wong, R.R. Hollins, G. Wang, J. Xie, Simultaneous delivery of multiple antimicrobial agents by biphasic scaffolds for effective treatment of wound biofilms, Adv. Healthc. Mater. 10 (2021) 2100135.
[10] G.L. Semenza, Defining the role of hypoxia-inducible factor 1 in cancer biology and therapeutics, Oncogene 29 (2010) 625–634.
[11] M. Guo, Y. Wang, B. Gao, B. He, Shark tooth-inspired microneedle dressing for intelligent wound management, ACS Nano 15 (2021) 15316–15327.
[12] G. Haddad, M. Kolling, U.A. Wegmann, A. Dettling, H. Seeger, R. Schmitt, I. Soerensen-Zender, H. Haller, A.D. Kistler, A. Dueck, S. Engelhardt, T. Thum, T. F. Mueller, R.P. Wuethrich, J.M. Lorenzen, Renal AAV2-mediated overexpression of long non-coding RNA H19 attenuates ischemic acute kidney injury through sponging of microRNA-30a-5p, J. Am. Soc. Nephrol. 32 (2021) 323–341.
[13] Q. Luo, D. Guo, G. Liu, G. Chen, M. Hang, M. Jin, Exosomes from MiR-126-overexpressing adscs are therapeutic in relieving acute myocardial ischaemic injury, Cell. Physiol. Biochem. 44 (2017) 2105–2116.
[14] V.S. Shilpa, R. Shams, K.K. Dash, V.K. Pandey, A.H. Dar, S.A. Mukarram, E. Harsanyi, B. Kovacs, Phytochemical properties, extraction, and pharmacological benefits of naringin: a review, Molecules 28 (2023) 5623.
[15] Y. Huang, M. Chen, Y. Shen, X. Shen, M. Li, Y. Li, Y. Liu, K. Cai, Z. Luo, Y. Hu, Bone-targeting cell membrane-engineered $CaCO_3$-based nanoparticles restore local bone

homeostasis for microenvironment-responsive osteoporosis treatment, Chem. Eng. J. 470 (2023) 144145.
[16] J. Deng, X. Wang, W. Zhang, L. Sun, X. Han, X. Tong, L. Yu, J. Ding, L. Yu, Y. Liu, Versatile hypoxic extracellular vesicles laden in an injectable and bioactive hydrogel for accelerated bone regeneration, Adv. Funct. Mater. 33 (2023) 2211664.
[17] L. Chuzeville, F. Boury, D. Duday, R. Anand, E. Moretto, J. Thomann, Eco-friendly processes for the synthesis of amorphous calcium carbonate nanoparticles in ethanol and their stabilisation in aqueous media, Green Chem. 24 (2022) 1270–1284.
[18] R. Kalluri, V.S. LeBleu, The biology, function, and biomedical applications of exosomes, Science 367 (2020) 640.
[19] L. Zhu, T. Tian, J. Wang, J. He, T. Chen, M. Pan, L. Xu, H. Zhang, X. Qiu, C. Li, K. Wang, H. Shen, G. Zhang, Y. Bai, Hypoxia-elicited mesenchymal stem cell-derived exosomes facilitates cardiac repair through miR-125b-mediated prevention of cell death in myocardial infarction, Theranostics 8 (2018) 6163–6177.
[20] S. Song, G. Zhang, X. Chen, J. Zheng, X. Liu, Y. Wang, Z. Chen, Y. Wang, Y. Song, Q. Zhou, HIF-1α increases the osteogenic capacity of ADSCs by coupling angiogenesis and osteogenesis via the HIF-1α/VEGF/AKT/mTOR signaling pathway, J. Nanobiotechnology 21 (2023) 257.
[21] W. Zhang, L. Wang, H. Guo, L. Chen, X. Huang, Dapagliflozin-loaded exosome mimetics facilitate diabetic wound healing by HIF-1α-mediated enhancement of angiogenesis, Adv. Healthcare Mater. 12 (2023) 2202751.
[22] M. Besnier, S. Gasparino, R. Vono, E. Sangalli, A. Facoetti, V. Bollati, L. Cantone, G. Zaccagnini, B. Maimone, P. Fuschi, D.D. Silva, M. Schiavulli, S. Aday, M. Caputo, P. Madeddu, C. Emanueli, F. Martelli, G. Spinetti, MiR-210 enhances the therapeutic potential of bone-marrow-derived circulating proangiogenic cells in the setting of limb ischemia, Mol. Ther. 26 (2018) 1694–1705.
[23] A. Ballini, S. Cantore, S. Scacco, D. Coletti, M. Tatullo, Mesenchymal stem cells as promoters, enhancers, and playmakers of the translational regenerative medicine 2018, Stem Cells Int. 2018 (2018) 6927401.
[24] D. Ando, M. Miyatsuji, H. Sakoda, E. Yamamoto, T. Miyazaki, T. Koide, Y. Sato, K. Izutsu, Mechanical characterization of dissolving microneedles: factors affecting physical strength of needles, Pharmaceutics 16 (2024) 200.
[25] S.I. Bisgaard, L.Q. Nguyen, K.L. Bogh, S.S. Keller, Dermal tissue penetration of in-plane silicon microneedles evaluated in skin-simulating hydrogel, rat skin and porcine skin, Biomater. Adv. 155 (2023) 213659.
[26] H. Chai, N. Chaudhari, R. Kornhaber, L. Cuttle, M. Fear, F. Wood, L. Martin, Chemical burn to the skin: a systematic review of first aid impacts on clinical outcomes, Burns 48 (2022) 1527–1543.
[27] S. Shen, D. Fan, Y. Yuan, X. Ma, J. Zhao, J. Yang, An ultrasmall infinite coordination polymer nanomedicine-composited biomimetic hydrogel for programmed dressing-chemo-low level laser combination therapy of burn wounds, Chem. Eng. J. 426 (2021) 130610.
[28] L. Zhou, T. Min, X. Bian, Y. Dong, P. Zhang, Y. Wen, Rational design of intelligent and multifunctional dressing to promote acute/chronic wound healing, ACS Appl. Bio Mater. 5 (2022) 4055–4085.
[29] Y. Liang, J. He, B. Guo, Functional hydrogels as wound dressing to enhance wound healing, ACS Nano 15 (2021) 12687–12722.
[30] T. Jia, D. Kuang, Z. Qi, G. Tan, X. Yang, S.C. Kundu, S. Lu, Silk fibroin/chitosan pH-sensitive controlled microneedles, J. Mater. Sci. 58 (2023) 17711–17725.
[31] R.M. Kratofil, P. Kubes, J.F. Deniset, Monocyte conversion during inflammation and injury, Arterioscler. Thromb. Vasc. Biol. 37 (2017) 35–42.
[32] P. Martin, Wound healing - aiming for perfect skin regeneration, Science 276 (1997) 75–81.
[33] Y. Dong, Z. Wang, ROS-scavenging materials for skin wound healing: advancements and applications, Front. Bioeng. Biotechnol. 11 (2023) 1304835.
[34] C. Zhang, T. Li, S. Yin, M. Gao, H. He, Y. Li, D. Jiang, M. Shi, J. Wang, L. Yu, Monocytes deposit migrasomes to promote embryonic angiogenesis, Nat. Cell Biol. 24 (2022) 1726–1738.
[35] D. Li, N. Wu, Mechanism and application of exosomes in the wound healing process in diabetes mellitus, Diabetes Res. Clin. Pract. 187 (2022) 109882.
[36] G. McKnight, J. Shah, R. Hargest, Physiology of the skin, Surgery 40 (2022) 8–12.
[37] K. Jyoti, G. Malik, M. Chaudhary, M. Sharma, M. Goswami, O.P. Katare, S.B. Singh, J. Madan, Chitosan and phospholipid assisted topical fusidic acid drug delivery in burn wound: strategies to conquer pharmaceutical and clinical challenges, opportunities and future panorama, Int. J. Biol. Macromol. 161 (2020) 325–335.
[38] G.C. Limandjaja, J.M. Belien, R.J. Scheper, F.B. Niessen, S. Gibbs, Hypertrophic and keloid scars fail to progress from the $CD34^{-}$/α-smooth muscle actin $(\alpha\text{-SMA})^{+}$ immature scar phenotype and show gradient differences in α-SMA and p16 expression, Br. J. Dermatol. 182 (2020) 974–986.